nature photonics

ARTICLES

https://doi.org/10.1038/s41566-019-0557-5

Bright high-colour-purity deep-blue carbon dot light-emitting diodes via efficient edge amination

Fanglong Yuan[1,2], Ya-Kun Wang[2], Geetu Sharma[3], Yitong Dong[2], Xiaopeng Zheng[4], Peicheng Li[1], Andrew Johnston[2], Golam Bappi[2], James Z. Fan[2], Hao Kung[1], Bin Chen[2], Makhsud I. Saidaminov[2,5], Kamalpreet Singh[3], Oleksandr Voznyy[3], Osman M. Bakr[4], Zheng-Hong Lu[1*] and Edward H. Sargent[2*]

Deep-blue light-emitting diodes (LEDs) (emitting at wavelengths of less than 450 nm) are important for solid-state lighting, vivid displays and high-density information storage. Colloidal quantum dots, typically based on heavy metals such as cadmium and lead, are promising candidates for deep-blue LEDs, but these have so far had external quantum efficiencies lower than 1.7%. Here we present deep-blue light-emitting materials and devices based on carbon dots. The carbon dots produce emission with a narrow full-width at half-maximum (about 35 nm) with high photoluminescence quantum yield (70% ± 10%) and a colour coordinate (0.15, 0.05) closely approaching the standard colour Rec. 2020 (0.131, 0.046) specification. Structural and optical characterization, together with computational studies, reveal that amine-based passivation accounts for the efficient and high-colour-purity emission. Deep-blue LEDs based on these carbon dots display high performance with a maximum luminance of 5,240 cd m^{-2} and an external quantum efficiency of 4%, notably exceeding that of previously reported quantum-tuned solution-processed deep-blue LEDs.

Deep-blue LEDs (< 450 nm) are important in energy-efficient solid-state lighting, vivid displays and high-density information storage[1–8]. However, deep-blue LEDs that combine bright and narrow-bandwidth emission with good external quantum efficiency (EQE) have proved challenging to produce. Colloidal semiconductor quantum dots, which typically rely on Cd^{2+} or Pb^{2+}, have emerged as candidates for efficient deep-blue LEDs on account of their solution-processibility, colour saturation, high brightness and wide spectral tunability. Table 1 summarizes the key optical parameters of quantum-tuned deep-blue emitters and the corresponding EQEs of solution-processing LEDs. Among conventional Cd^{2+}-based colloidal semiconductor quantum dots, the EQEs of blue and sky-blue LEDs have been improved to over 10%[9–14]. However, unfortunately, the EQEs of the best deep-blue colloidal semiconductor quantum dots remain below 1.7%. Perovskite-based (Pb^{2+}-based emitters, including two-dimensional and colloidal semiconductor quantum dots) deep-blue LEDs have also generated intense interest in recent years, but have remained below 0.3% EQE (Table 1)[15–20]. Regulations on the use of Cd^{2+} and Pb^{2+} in consumer electronics add a further impediment to adoption.

Carbon dots (CDs) are generally comprised of abundant elements and are free of heavy metals[21–31]. In the past few years, much progress has been made in designing and synthesizing efficient and tunable fluorescent CDs emitting from the deep-blue (430 nm) to the near-infrared (NIR, 730 nm)[21–25,28–30,32] part of the spectrum. Devices based on these CDs, such as electroluminescent LEDs, phosphor-converted LEDs and lasers, have been demonstrated[22–26,32–38]. However, conventional CDs have so far been limited by their relatively broad luminescence in the deep-blue region (full-width at half-maximum, FWHM, > 80 nm; see Extended Data Fig. 1a). The mechanism underpinning the broad fluorescence spectra of these CDs remains largely unexplored. Broad fluorescence spectra cannot be explained via dot size polydispersity alone, but also include a considerable homogeneous broadening component[25,39]. Different oxygen-containing functional groups such as carboxyl, carbonyl and epoxy groups at the edge or basal plane sites in CDs influence the photoluminescence (PL) spectra: they may function as transient trap states, that is, defects formed under excitation. These have been reported to capture photogenerated charge carriers through large-amplitude vibrations and distortions, thus lowering PL quantum yield[40,41]. These large distortions could also potentially dynamically affect the bandgap of the CDs as well as contribute to inhomogeneous broadening of monodisperse CD ensembles via differences in the arrangement of the functional groups on the edges and the basal plane.

Here we report that wave-function polarization arising from the thermal vibrations of oxygen-containing functional groups contributes to spectral broadening. We then develop a synthesis of CDs that aims to reduce the density of these functional groups. As a result, we achieve high-colour-purity, deep-blue narrow-bandwidth emissive CDs (FWHM of 35 nm) with a PL quantum yield of 70% ± 10%. The deep-blue emission provides a colour coordinate of (0.15, 0.05), approaching the standard colour Rec. 2020 (0.131, 0.046) specification. We report deep-blue LEDs with maximum luminance (L_{max}) exceeding 5,000 cd m^{-2} and a maximum EQE of 4%.

Results

Origins of spectral broadening. We sought, using density functional theory calculations, to explore the effect of oxygen-containing functional groups on spectral linewidth. The electronic coupling to

[1]Department of Materials Science and Engineering, University of Toronto, Toronto, Ontario, Canada. [2]Department of Electrical and Computer Engineering, University of Toronto, Toronto, Ontario, Canada. [3]Department of Physical and Environmental Sciences, University of Toronto, Toronto, Ontario, Canada. [4]Division of Physical Sciences and Engineering, King Abdullah University of Science and Technology (KAUST), Thuwal, Kingdom of Saudi Arabia. [5]Present address: Department of Chemistry and Electrical and Computer Engineering, Centre for Advanced Materials and Related Technologies (CAMTEC), University of Victoria, Victoria, British Columbia, Canada. *e-mail: zhenghong.lu@utoronto.ca; ted.sargent@utoronto.ca

Table 1 | Key optical parameters of quantum-tuned deep-blue emitters for LED applications

Materials category and examples		Quantum yield (%)	Emission peak (nm)	Commission Internationale de l'Eclairage	EQE (%)	Brightness (cd m^{-2})	Reference
Cd-based quantum dots (toxic)	CdSe/ZnS	73	475 (sky blue)	(0.12, 0.15)	8.05	62,600	9
	$Cd_{1-x}Zn_xS/ZnS$	70	437	(0.17, 0.02)	1.7	2,200	13
Pb-based (toxic) two-dimensional perovskite	$(PEA)_2PbBr_4$	26	410	NA	0.04	NA	16
	$(PEA)_2PbBr_4$	15–25	410	NA	0.31	140	17
	$(BA)_2(MA)_{n-1}Pb_nBr_{3n+1}$	<1	450	(0.21, 0.17)	0.0054	1	18
Perovskite quantum dots	$CsPb(Br_{1-x}Cl_x)_3$	80	455	(0.20, 0.04)	0.07	742	19
Cd-free, Pb-free (non-toxic) carbon dots		41	474	(0.22, 0.27)	NA	570	49
High-colour-purity deep-blue carbon dots		80	433 (deep blue)	(0.15, 0.05)	4.04	5,240	This work

CIE, Commission Internationale de l'Eclairage. n is a positive integer, ≥1, and $0 < x < 1$.

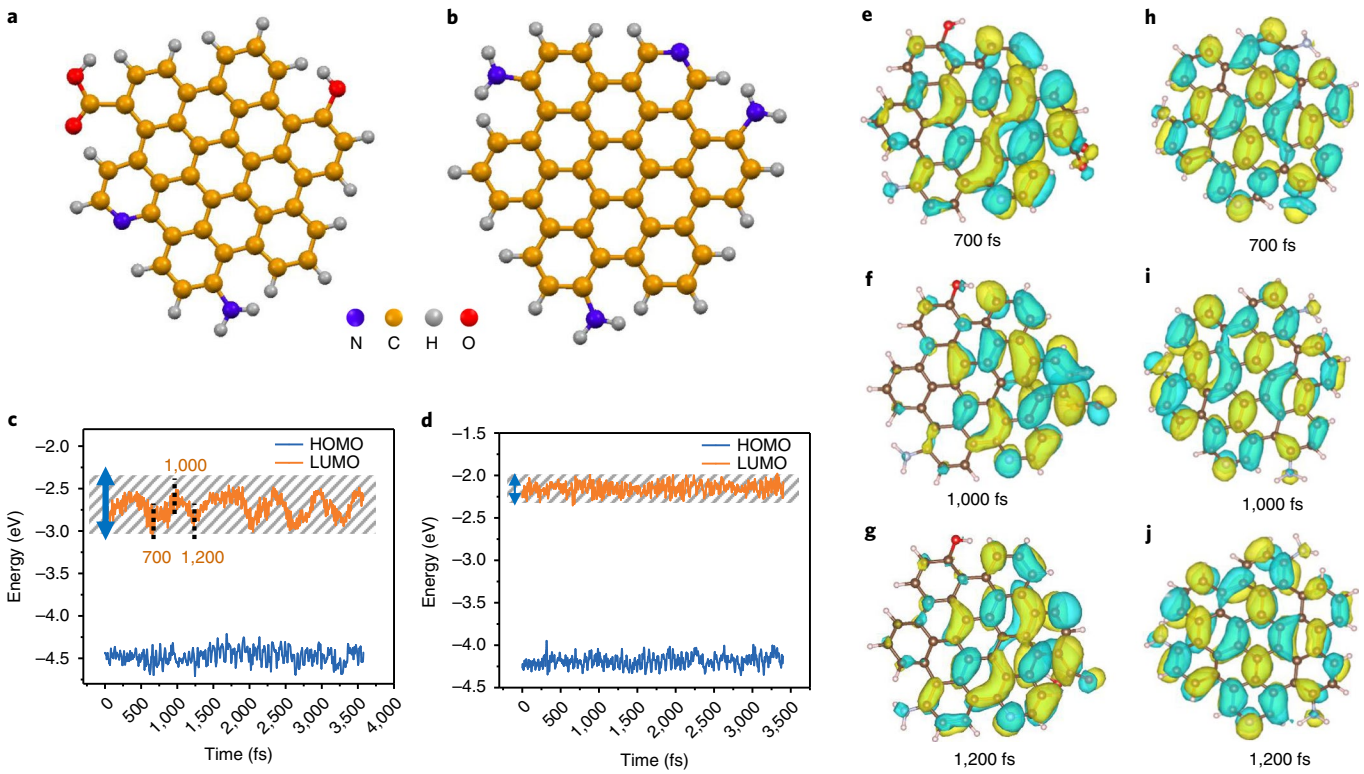

Fig. 1 | Density functional theory calculations on model CDs. a, **b**, Molecular structure of COOH-CD (**a**) and NH_2-CD (**b**). **c**, **d**, The bandgap fluctuations of COOH-CD (**c**) and NH_2-CD (**d**). **e**–**j**, The wavefunctions of COOH-CD and NH_2-CD at different time intervals, such as 700 fs (**e**, **h**), 1,000 fs (**f**, **i**) and 1,200 fs (**g**, **j**).

molecular vibrations and distortions is believed to broaden emission spectra, particularly in small dots[42–44]. We carried out molecular dynamics simulations using the Vienna Ab-initio Simulation Package (VASP), tracking the vibrations of the bandgap for several model CDs terminated with different functional groups. The first, denoted COOH-CD (Fig. 1a), is functionalized with OH, COOH and NH_2, corresponding to previously reported CDs. The second model, NH_2-CD (Fig. 1b), is functionalized with NH_2 functional groups only. We observe low-frequency vibrations in the lowest unoccupied molecular orbital (LUMO) of the COOH-CD, which are not seen in that of the NH_2-CD (Fig. 1c, d). Large distortions in the basal plane are also observed in COOH-CD (Extended Data Fig. 2). Closer inspection of the wavefunctions reveals a strong polarization effect due to the COOH functional group, whose rotation relative to the basal plane affects the degree of wavefunction localization (Fig. 1e–g) and, consequently, produces bandgap fluctuations. The bandgap fluctuations of NH_2-CD are smaller (Fig. 1d), and the wavefunctions are more delocalized (Fig. 1h–j). The variations in the epoxy group number and their arrangement on CDs may contribute to a spread of bandgap values (Supplementary Fig. 1). We propose from these initial studies that eliminating the oxygen-containing functional groups could contribute to narrow-linewidth emission.

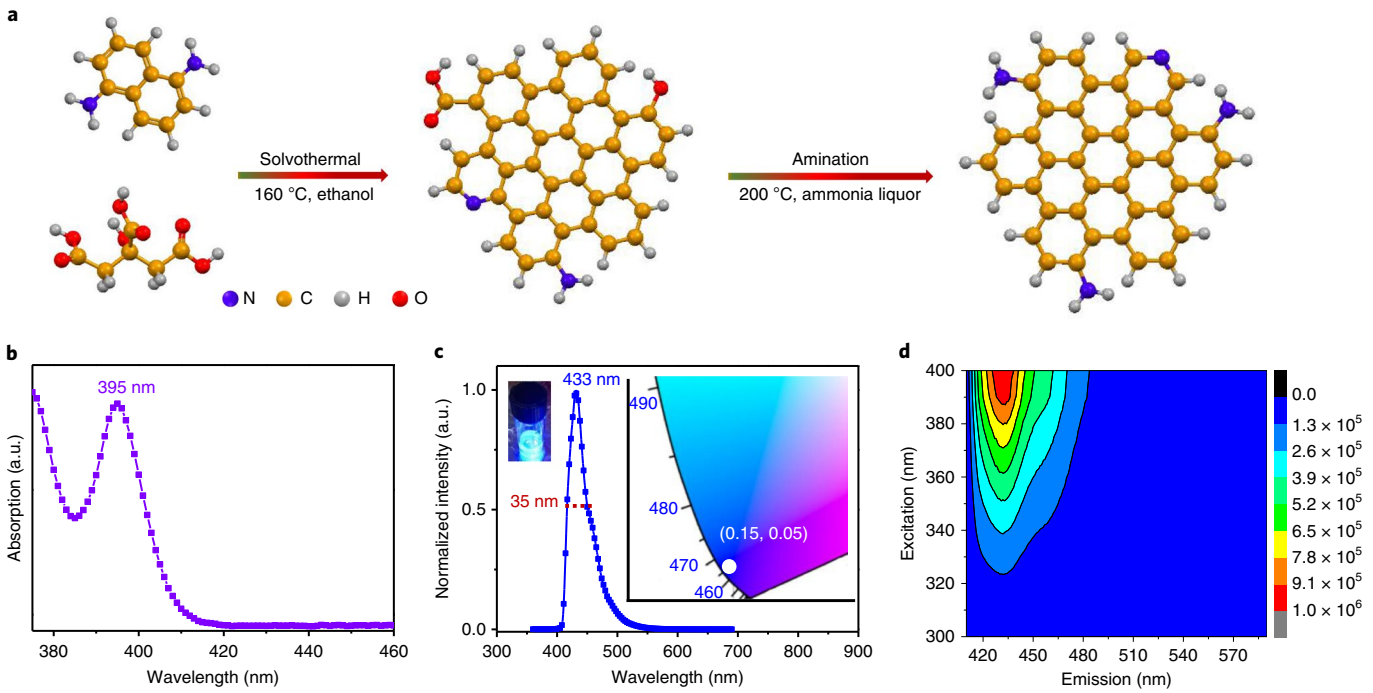

Fig. 2 | Synthesis and optical properties of HCP-DB-CDs. a, Schematic showing the synthetic strategy. **b**–**d**, Absorption (**b**), PL (**c**), and excitation-emission spectra (**d**) of HCP-DB-CDs. The colour scale is in arbitrary units.

Synthesis and optical properties of deep-blue CDs. Eliminating oxygen-containing functional groups while retaining solution processibility requires surface engineering of CDs. We developed a two-step method for the synthesis of high-colour-purity deep-blue CDs (HCP-DB-CDs) (Fig. 2a). First, the CDs functionalized with OH, COOH and NH_2 are synthesized through solvothermal treatment using citric acid and diaminonaphthalene. Citric acid produces the structural skeleton of CDs during the process of solvothermal treatment due to its low carbonization temperature, and the diaminonaphthalene is used to introduce nitrogen into the structure of CDs, and also to passivate the surface of CDs with amino groups to reduce the trap states and improve the PL quantum yield. We follow this with an additional surface amination step using ammonia liquor and hydrazine hydrate under high temperature to further eliminate the oxygen-containing functional groups. The HCP-DB-CDs were purified via silica column chromatography using a mixture of dichloromethane and methanol as the eluent to remove the byproducts and unreacted precursors, which could limit carrier injection in LEDs.

The absorption spectra of HCP-DB-CDs have a narrow excitonic absorption peak centred at 395 nm (Fig. 2b). The emission peak is centred at about 433 nm with a FWHM of 35 nm (Fig. 2c), much smaller than that of the FWHM >80 nm in conventional deep-blue CDs (C-DB-CDs) (Extended Data Fig. 1b)[21,24,28,30–34,38–40]. The deep-blue emission has a colour coordinate of (0.15, 0.05) closely approaching the Rec. 2020 (0.131, 0.046) specification (Extended Data Fig. 1c). These improve upon the colour purity of deep-blue Cd^{2+}/Pb^{2+}-based emitters (Table 1)[6,9–19]. The narrow emission peak of HCP-DB-CDs is retained over a wide excitation wavelength range (Fig. 2d, Extended Data Fig. 3a), consistent with the PL arising from direct band-to-band recombination. The PL excitation spectra of HCP-DB-CDs show a peak at 394 nm (Extended Data Fig. 3b), and agrees well with the absorption peak (Fig. 2b), which demonstrates the bandgap emission properties of HCP-DB-CDs. For C-DB-CDs treated at 200 °C for 1 h without adding amination reagents, the emission spectra show a large FWHM of 62 nm (Extended Data Fig. 1d), which indicates that the amination is responsible for the reduced FWHM of the emission spectra. We then studied the stability of HCP-DB-CDs under ambient conditions: the emission intensity and spectra show no obvious change after being stored for six months (Extended Data Fig. 3c). The HOMO energy level was determined by means of ultraviolet photoelectron spectroscopy (UPS) to be −5.60 eV (Extended Data Fig. 4), and the LUMO is −2.64 eV, based on the optical bandgap energy (2.96 eV) and the highest unoccupied molecular orbital (HOMO) energy level.

To gain further insight into exciton recombination dynamics, we measured the time-resolved PL spectra of HCP-DB-CDs at 433 nm emission wavelength and 374 nm excitation wavelength (Fig. 3a). These show monoexponential decay with fluorescence lifetime of 7 ns, different from the two-exponential decay of C-DB-CDs with average fluorescence lifetime of 4.8 ns (Extended Data Fig. 1e). The monoexponential decay is consistent with minimal trap recombination[21,29–31,34,37–40]. The quantum yield is 70% ± 10%, which is among the highest values for CDs reported to date, appreciably higher than that of 45% ± 5% for C-DB-CDs, and comparable to the best Cd^{2+}/Pb^{2+}-based emitters. The high quantum yield is ascribed to the efficient edge amination, which decreases the amount of defects of HCP-DB-CDs and thus suppresses non-radiative pathways. The quantum yield is determined by the ratio of the radiative recombination rate (k_{rad}) to the sum of radiative and non-radiative (k_{non}) recombination rates (k_{tot}) described by the following equation:

$$\mathrm{PLQY} = \frac{k_{rad}}{k_{tot}} = \frac{k_{rad}}{k_{rad} + k_{non}}$$

We estimate k_{tot} to be 1.4×10^8 s^{-1}, and k_{rad} to be 1.2×10^8 s^{-1}. To acquire more intrinsic characteristics of the photogenerated excitons in the high-colour-purity emission of HCP-DB-CDs, temperature-dependent PL spectra were also recorded. As seen in Fig. 3b, a pseudocolour map of the temperature-dependent PL spectra shows a slight increase in integrated PL intensity with decreasing temperature from 300 K to 90 K (Fig. 3c), ascribed to reduced exciton dissociation and nonradiative trapping[25]. To extract the exciton binding

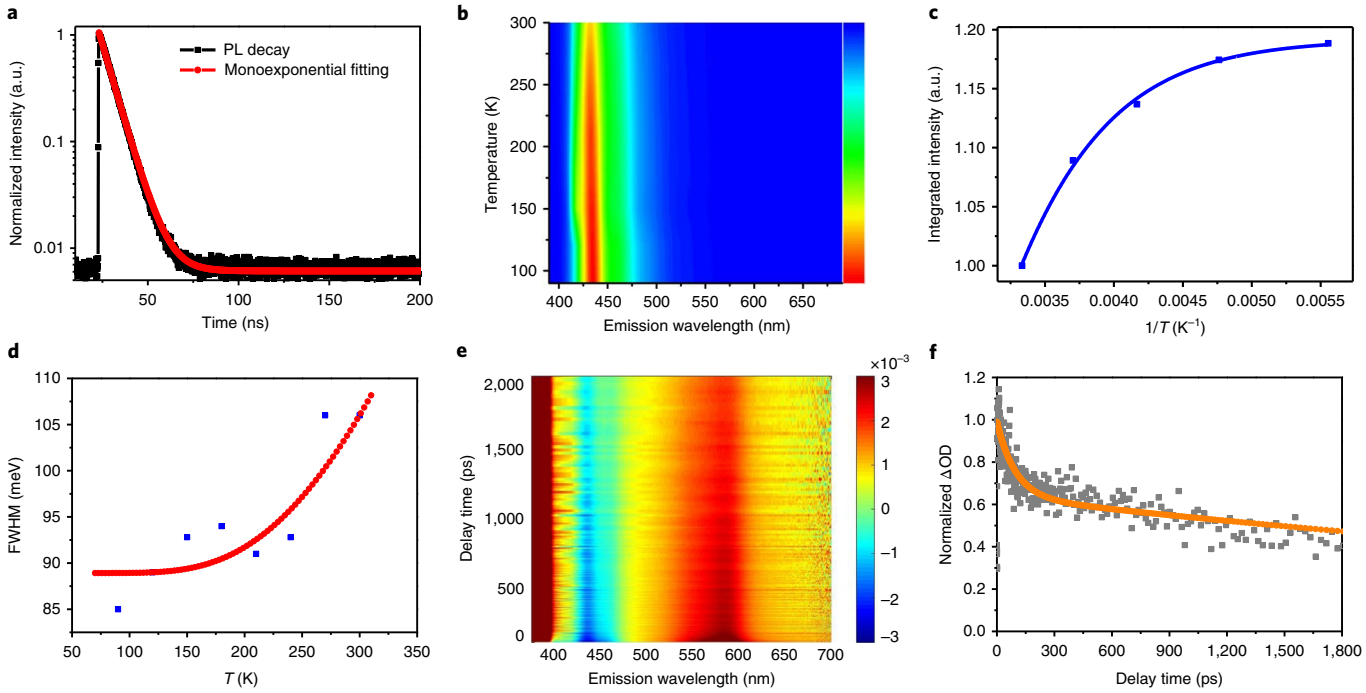

Fig. 3 | Time-resolved PL spectra, low temperature-dependent PL spectra and femtosecond transient absorption (TA) spectra of HCP-DB-CDs. **a**, **b**, Time-resolved PL spectra (**a**) and pseudocolour map of low temperature-dependent PL spectra (**b**). **c**, **d**, Integrated PL emission intensity (**c**) and the FWHM as a function of temperature (**d**). **e**, Two-dimensional pseudocolour map of TA spectra of HCP-DB-CDs expressed in ΔOD (the change of the absorption intensity of the sample after excitation) as a function of both delay time and probe wavelength excited at 355 nm. **f**, Kinetic trace at probe wavelength 430 nm.

energy, we plot in Fig. 3c the integrated PL emission intensity as a function of inverse temperature:

$$I(T) = \frac{I_0}{1 + Ae^{-\frac{E_b}{K_B T}}}$$

where I_0 is the integrated emission intensity at 0 K, E_b is the exciton binding energy, and k_B is the Boltzmann constant. The HCP-DB-CDs have a large exciton binding energy of 150 ± 14 meV.

The FWHM of the PL spectra decreased from 106 meV to 85 meV when the temperature was decreased from 300 K to 90 K (Fig. 3d, Supplementary Figs. 2, 3). The narrowed FWHM of the HCP-DB-CDs at low temperature is explained by reduced electron–phonon coupling due to reduced structural vibrations and distortions at lower temperatures[45–47]. To extract the electron–phonon coupling strength, we fitted the temperature dependence of the FWHM using the equation:

$$\mathrm{FWHM(T)} = \frac{A}{\exp(\frac{E_{ph}}{k_B T}) - 1} + \mathrm{c}$$

containing the longitudinal optical (LO) phonon contribution, which includes the Bose–Einstein distribution term and where E_{ph} is the LO phonon energy and the term A denotes the coupling strength. The inhomogeneous broadening term C is unrelated to thermal effects, and correspomnds to the FWHM at low temperatures, where not much thermal broadening occurs. The fit shows that reduced LO phonon coupling can account for the observed narrowed FWHM. The LO phonon energy and coupling strength are 40 meV and 52 meV, respectively.

To scrutinize further the bright and high-colour-purity emission of the HCP-DB-CDs from the perspective of transfer and recombination dynamics of photogenerated charges, we carried out femtosecond TA using 355 nm excitation. The TA spectra of HCP-DB-CDs are depicted in Fig. 3e with the probe in the 360–700 nm range and scan delay time from 0.2 ps to 2 ns. A strong ground-state bleaching signal centred at 395 nm is observed (Extended Data Fig. 3d–f). This bleach recovers in around 1 ps, indicating rapid charge transfer from the excited state to the emissive state, which is different from that of the femtosecond TA spectra of C-DB-CDs (Extended Data Fig. 1f). A negative peak centred at about 430 nm rises, commensurate with decay of the ground-state bleaching at 395 nm (Extended Data Fig. 3d–f). The positive features at 377 nm and 580 nm are ascribed to the excited state absorption (Fig. 3e). We followed the change of A in the time domain, ΔA, at 430 nm (Fig. 3f). The decay curve was fitted using bi-exponential function, with lifetimes of 96 ps and 6 ns. The fast-decay and long-decay components are associated with non-radiative and radiative recombinations. The small amplitude of this fast-decay component agrees with the observed bright emission.

Structural characterization. Transmission electron microscopy (TEM) images reveal that the HCP-DB-CDs are nanodots (Extended Data Fig. 5a) with average lateral size 2.4 nm (Extended Data Fig. 5b). High-resolution TEM shows HCP-DB-CDs with a lattice spacing of 0.21 nm, consistent with the (100) lattice spacing of graphene (Extended Data Fig. 5a)[24,28,32]. X-ray powder diffraction of HCP-DB-CDs shows a narrow (002) peak centred at 26° in contrast to the broad (002) peak of C-DB-CDs (Extended Data Fig. 5c)[21,24,28,30–34,38–40]. The higher degree of graphitization of the HCP-DB-CDs is reflected in their Raman spectra (Extended Data Fig. 5d), where the crystalline G band at 1,616 cm^{-1} is stronger than the disordered D band at 1,365 cm^{-1}, with a G to D intensity ratio (I_G / I_D) of 1.64, higher than the value of 1.15 of C-DB-CDs.

Fourier transform infrared and X-ray photoelectron spectroscopy (XPS) spectra show that, following amination, the HCP-DB-CDs

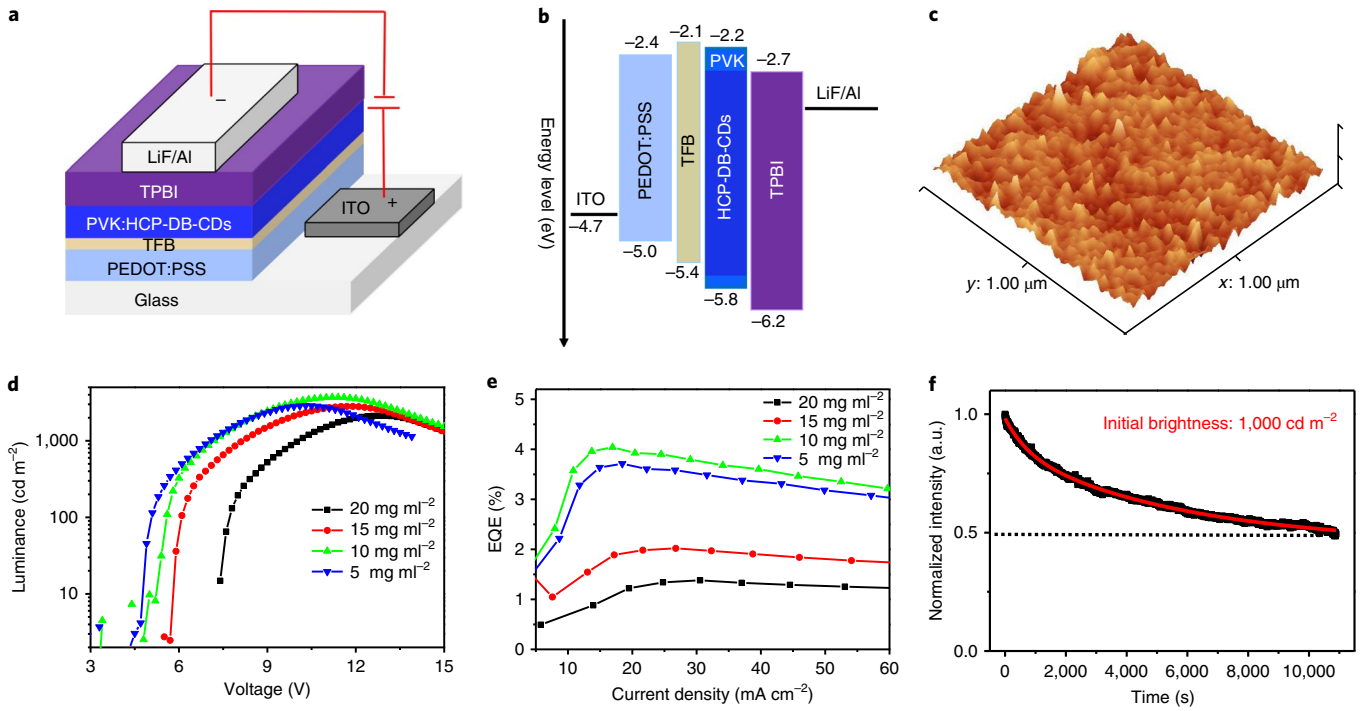

Fig. 4 | LED structure, energy diagram and performance. a, **b**, Device structure (**a**), energy level diagram (**b**) of HCP-DB-CD-based LEDs. **c**, AFM height image of PVK:HCP-DB-CDs film. **d**–**f**, Luminance–voltage (**d**) and EQE–current density (**e**) characteristics, and device stability (**f**) of HCP-DB-CD-based LEDs.

are passivated with electron-donating amino groups at the surface, and no signal associated with oxygen-containing functional groups is detected. The stretching vibration bands of C=O (1,710 cm^{-1}), O-H and COOH (broad band at 3,400 cm^{-1}) disappear after amination, while the signals of the stretching vibration bands of N-H (two peaks at 3,340 cm^{-1} and 3,392 cm^{-1}), C-N (1,433 cm^{-1}) increase in HCP-DB-CDs compared with that of C-DB-CDs (Extended Data Fig. 5e). The loss of oxygen-containing functional groups seen in C-DB-CDs is further revealed by XPS measurements (Extended Data Fig. 5f). After amination, the oxygen content became unobservable above the baseline, while the nitrogen content increased from 5.8% to 8.6%. The signals of oxygen-containing functional groups such as C-O (285.95 eV) and C=O/COOH (289.4 eV) in high-resolution C 1*s* XPS spectra of C-DB-CDs (Extended Data Fig. 6a) decreased in HCP-DB-CDs (Extended Data Fig. 6b) after amination. The high-resolution N 1*s* XPS spectra also demonstrate that the nitrogens are mainly in the form of amino groups with a small amount in the form of pyridine (Extended Data Fig. 6c,d).

Deep-blue LED devices. We sought to incorporate HCP-DB-CDs in LEDs. We use an indium tin oxide (ITO) glass substrate anode, a poly(3,4-ethylenedioxythiophene):poly(styrene-sulfonate) (PEDOT:PSS) hole injection layer, a poly (9,9-dioctylfluorene-co-N-(4-(3-methylpropyl)) diphenylamine) (TFB) hole transport layer, an active HCP-DB-CDs blended poly(*N*-vinyl carbazole) (PVK) emission layer, a 1,3,5-tris(*N*-phenylbenzimidazol-2-yl) benzene (TPBI) electron transport layer (ETL), and a LiF/Al double-layered cathode (Fig. 4a). As illustrated in the energy level diagram of the HCP-DB-CD-based LEDs shown in Fig. 4b, the HOMO and LUMO energy levels of HCP-DB-CDs are located within those of the PVK, and have a small energy barrier for charge injection from both electrodes to the PVK host[47,48]. The thicknesses of the PEDOT:PSS, the TFB and the active emissive layer of the device are 20 nm, 10 nm and 20 nm, respectively (cross-sectional TEM image, Extended Data Fig. 7a). PVK is used as the host material owing to its favourable film-forming properties, and also disperses the HCP-DB-CDs and prevents aggregation-induced emission quenching. The SEM image reveals a uniform film of active emission layer material with good film coverage and without obvious pinholes (Extended Data Fig. 7b). Atomic force microscope (AFM) measurements also show that the HCP-DB-CD blended PVK film has a small root-mean-square roughness of 0.5 nm (Fig. 4c, Extended Data Fig. 7c). The PL emission peaks of PVK:HCP-DB-CD films (the concentration of HCP-DB-CDs is in the range from 1.5–4.0 mg ml^{-1}) are at 440 nm, distinct from those of the PVK film at 390 nm, indicating efficient energy transfer from PVK to HCP-DB-CD (Extended Data Fig. 7d). The emission peaks of the films redshifted 7 nm compared with the emission peak of the solution (433 nm, 0.2 mg ml^{-1}) (Extended Data Fig. 7e). The bright deep-blue emission with colour coordinates of (0.15, 0.07) from the PVK:HCP-DB-CDs film (Supplementary Fig. 4) is observed under ultraviolet light, while almost no emission from the PVK film was observable to the naked eye (Extended Data Fig. 7d,f, Supplementary Figs. 5–7).

The electroluminescence (EL) spectra of the HCP-DB-CD-based LEDs remain at 440 nm across the range of voltage biases explored herein, and are in good agreement with the PL emission peaks of HCP-DB-CD measured films, indicating efficient energy transfer from PVK to HCP-DB-CDs (Extended Data Fig. 8a,b). Luminance and current density curves as a function of applied voltage for the HCP-DB-CD-based LEDs prepared with different concentrations of PVK:HCP-DB-CDs are shown in Fig. 4d and Extended Data Fig. 8c. The performance is summarized in Supplementary Table 1. L_{max} reaches 5,240 cd m^{-2} for deep-blue LEDs (Extended Data Fig. 9a), one order of magnitude higher than previously reported blue CD-based LEDs (Extended Data Table 1)[24,33,38,49]. The maximum EQE is 4%, corresponding to a current efficiency of 2.6 cd A^{-1} (the corresponding L_{max} is 3,715 cd m^{-2}) (Fig. 4d,e), exceeding that of Cd^{2+}/Pb^{2+}-based deep-blue LEDs (Table 1)[13,16–19]. The hole-transport TFB polymer also contributed to performance owing to improved charge injection and charge balance in the

emission layer. Without TFB, L_{max} and maximum EQE are 954 cd m^{-2} and 1.7% (Extended Data Fig. 9b). After operating for 3 h, about 50% of initial luminance (L_0 1,000 cd m^{-2}, constant current density of 40 mA cm^{-2}) is retained (Fig. 4f), and the EL spectra are almost unchanged (Extended Data Fig. 8d, 9c).

In sum, we have reported the demonstration of high-colour-purity deep-blue emission from CDs (FWHM of 35 nm) with a quantum yield of 70% ± 10%. Amination, aimed at eliminating oxygen-containing functional groups, enables efficient high-colour-purity emission. With an L_{max} of 5,240 cd m^{-2} and a maximum EQE of 4%, deep-blue LEDs based on these high-colour-purity CDs substantially outperform deep-blue LEDs based on Cd^{2+}/Pb^{2+}-comprising materials.

Online content

Any methods, additional references, Nature Research reporting summaries, source data, extended data, supplementary information, acknowledgements, peer review information; details of author contributions and competing interests; and statements of data and code availability are available at https://doi.org/10.1038/s41566-019-0557-5.

Received: 18 August 2019; Accepted: 28 October 2019;
Published online: 09 December 2019

References

1. Forrest, S. R. et al. Highly efficient phosphorescent emission from organic electroluminescent devices. *Nature* **395**, 151–154 (1998).
2. Yang, X., Xu, X. & Zhou, G. Recent advances of the emitters for high performance deep-blue organic light-emitting diodes. *J. Mater. Chem. C.* **3**, 913–944 (2015).
3. Ponce, F. A. & Bour, D. P. Nitride-based semiconductors for blue and green light-emitting devices. *Nature* **386**, 351–359 (1997).
4. Shirasaki, Y., Supran, G. J., Bawendi, M. G. & Bulović, V. Emergence of colloidal quantum-dot light-emitting technologies. *Nat. Photon.* **7**, 933-–9933 (2013).
5. Dai, X. et al. Solution-processed, high-performance light-emitting diodes based on quantum dots. *Nature* **515**, 96–99 (2014).
6. Shen, H. et al. High-efficiency, low turn-on voltage blue-violet quantum-dot based light-emitting diodes. *Nano Lett.* **15**, 1211–1216 (2015).
7. Wang, Q. et al. Management of charges and excitons for high-performance white organic light-emitting diodes. *Chem. Soc. Rev.* **39**, 2387–2398 (2010).
8. Yuan, F. et al. Shining carbon dots: Synthesis and biomedical and optoelectronic applications. *Nano Today* **11**, 565–586 (2016).
9. Shen, H. et al. Visible quantum dot light-emitting diodes with simultaneous high brightness and efficiency. *Nat. Photon.* **13**, 192–197 (2019).
10. Qian, L., Zheng, Y., Xue, J. & Holloway, P. H. Stable and efficient quantum dot light-emitting diodes based on solution-processed multilayer structures. *Nat. Photon.* **5**, 543–548 (2011).
11. Yang, Y. et al. High-efficiency light-emitting devices based on quantum dots with tailored nanostructures. *Nat. Photon.* **9**, 259–266 (2015).
12. Lee, K. et al. Highly efficient, colour-pure, colour-stable blue quantum dot light-emitting devices. *ACS Nano* **7**, 7295–7302 (2013).
13. Kwak, J. et al. Bright and efficient full-colour colloidal quantum dot light-emitting diodes using an inverted device structure. *Nano Lett.* **12**, 2362–2366 (2012).
14. Shen, H. et al. High-efficiency deep-blue light-emitting diodes by using high quality $Zn_xCd_{1-x}S$/ZnS core/shell quantum dots. *Adv. Funct. Mater.* **24**, 2367–2373 (2014).
15. Stranks, S. D. & Snaith, H. J. Metal-halide perovskites for photovoltaic and light-emitting devices. *Nat. Nanotech.* **10**, 391–402 (2015).
16. Liang, D. et al. Colour-pure violet-light-emitting diodes based on layered lead halide perovskite nanoplates. *ACS Nano* **10**, 6897–6904 (2016).
17. Deng, W. et al. 2D Ruddlesden–Popper perovskite nanoplate based deep-blue light-emitting diodes for light communication. *Adv. Funct. Mater.* **29**, 1903861 (2019).
18. Chen, Z. et al. High-performance colour-tunable perovskite light emitting devices through structural modulation from bulk to layered film. *Adv. Mater.* **29**, 1603157 (2017).
19. Hou, S. et al. Efficient blue and white perovskite light-emitting diodes via manganese doping. *Joule* **2**, 2421–2433 (2018).
20. Jang, Y. et al. Spectra stable blue perovskite light-emitting diodes. *Nat. Commun.* **10**, 1868 (2019).
21. Jiang, K. et al. Red, green, and blue luminescence by carbon dots: full-colour emission tuning and multicolour cellular imaging. *Angew. Chem. Int. Ed.* **54**, 5360–5363 (2015).
22. Qu, S. N. et al. Toward efficient orange emissive carbon nanodots through conjugated sp^2-domain controlling and surface charges engineering. *Adv. Mater.* **28**, 3516–3521 (2016).
23. Wang, Z. F. et al. 53% efficient red emissive carbon quantum dots for high colour rendering and stable warm white-light-emitting diodes. *Adv. Mater.* **29**, 1702910 (2017).
24. Yuan, F. L. et al. Bright multicolour bandgap fluorescent carbon quantum dots for electroluminescent light-emitting diodes. *Adv. Mater.* **29**, 1604436 (2017).
25. Yuan, F. et al. Engineering triangular carbon quantum dots with unprecedented narrow bandwidth emission for multicoloured LEDs. *Nat. Commun.* **9**, 2249 (2018).
26. Choi, H. et al. Versatile surface plasmon resonance of carbon-dot-supported silver nanoparticles in polymer optoelectronic devices. *Nat. Photon.* **7**, 732–738 (2013).
27. Lim, S. et al. Carbon quantum dots and their applications. *Chem. Soc. Rev.* **44**, 362–381 (2015).
28. Wang, L. et al. Gram-scale synthesis of single-crystalline graphene quantum dots with superior optical properties. *Nat. Commun.* **5**, 5357 (2014).
29. Sun, Y.-P. et al. Quantum-sized carbon dots for bright and colourful photoluminescence. *J. Am. Chem. Soc.* **128**, 7756–7757 (2006).
30. Zhu, S. et al. Highly photoluminescent carbon dots for multicolour patterning, sensors, and bioimaging. *Angew. Chem. Int. Ed.* **52**, 3953–3957 (2013).
31. Li, H. et al. Water-soluble fluorescent carbon quantum dots and photocatalyst design. *Angew. Chem. Int. Ed.* **49**, 4430–4434 (2010).
32. Jia, H. R. et al. Electroluminescent warm white light-emitting diodes based on passivation enabled bright red bandgap emission carbon quantum dots. *Adv. Sci.* **6**, 1900397 (2019).
33. Zhang, X. et al. Colour-switchable electroluminescence of carbon dot light-emitting diodes. *ACS Nano* **7**, 11234–11241 (2013).
34. Yang, H. et al. Hydrophobic carbon dots with blue dispersed emission and red aggregation-induced emission. *Nat. Commun.* **10**, 1789 (2019).
35. Yuan, F. et al. Highly efficient and stable white LEDs based on pure red narrow bandwidth emission triangular carbon quantum dots for wide-colour gamut backlight displays. *Nano Res.* **12**, 1669–1674 (2019).
36. Yuan, F. et al. Ultrastable and low-threshold random lasing from narrow-bandwidth-emission triangular carbon quantum dots. *Adv. Opt. Mater.* **7**, 1801202 (2019).
37. Luo, Z. et al. Microwave-assisted preparation of white fluorescent graphene quantum dots as a novel phosphor for enhanced white-light-emitting diodes. *Adv. Funct. Mater.* **26**, 2739–2744 (2016).
38. Kwon, W. et al. Electroluminescence from graphene quantum dots prepared by amidative cutting of tattered graphite. *Nano Lett.* **14**, 1306–1311 (2014).
39. Ding, H. et al. Solvent-controlled synthesis of highly luminescent carbon dots with a wide colour gamut and narrowed emission peak widths. *Small* **14**, 1800612 (2018).
40. Li, H. et al. Full-colour light-emitting carbon dots with a surface-state-controlled luminescence mechanism. *ACS Nano* **10**, 484–491 (2016).
41. Yuan, Z. et al. One-dimensional organic lead halide perovskites with efficient bluish white-light emission. *Nat. Commun.* **8**, 14051 (2017).
42. Beyler, A. et al. Direct observation of rapid discrete spectral dynamics in single colloidal CdSe-CdS core-shell quantum dots. *Phys. Rev. Lett.* **111**, 177401 (2013).
43. Voznyy, O. et al. Computational study of magic-size CdSe clusters with complementary passivation by carboxylic and amine ligands. *J. Phys. Chem. C.* **120**, 10015–10019 (2016).
44. Povie, G. et al. Synthesis of a carbon nanobelt. *Science* **356**, 172–175 (2017).
45. Manser, J. S., Christians, J. A. & Kamat, P. V. Intriguing optoelectronic properties of metal halide perovskites. *Chem. Rev.* **116**, 12956–13008 (2016).
46. Adam, D. W. et al. Electron-phonon coupling in hybrid lead halide perovskites. *Nat. Commun.* **7**, 11755 (2016).
47. Balan, A. D. et al. Effect of thermal fluctuations on the radiative rate in core/shell quantum dots. *Nano Lett.* **17**, 1629–1636 (2017).
48. Kim, J. K. et al. Origin of white electroluminescence in graphene quantum dots embedded host/guest polymer light emitting diodes. *Sci. Rep.* **5**, 11032 (2015).
49. Xu, J. et al. Ultrahigh brightness carbon dot–based blue electroluminescent LEDs by host–guest energy transfer emission mechanism. *Adv. Opt. Mater.* **6**, 1800181 (2018).

Methods

Synthesis of CDs. The HCP-DB-CDs were synthesized by solvothermal treatment of citric acid and diaminonaphthalene. In a typical synthesis, citric acid (100 mg) and diaminonaphthalene (20 mg) were dissolved in ethanol (15 ml). After 10 min of sonication, the clear precursor solution was then transferred to a poly(tetrafluoroethylene) (Teflon)-lined autoclave (25 ml) and heated at 160 °C for 6 h. After the reaction, the solution was cooled to room temperature, either using water or air. For surface amination, 3 ml of ammonia liquor and 0.01 ml hydrazine hydrate were added to the obtained CD solution, and then solvothermal synthesis was carried out at 200 °C for 1 h. After the reaction, the reactors were cooled to room temperature by water or air. The C-DB-CDs were obtained without the process of surface amination. The CDs were purified via silica column chromatography several times using a mixture of dichloromethane and methanol as the eluent.

Optical characterization. Steady-state PL spectra were recorded using a Horiba Fluorolog system equipped with a single grating; a monochromatized Xe lamp was used as the excitation source. PL quantum yield measurements were made by coupling a Quanta-Phi integrating sphere to the Horiba Fluorolog system with optical fibre bundles. Both excitation and emission spectra were collected for the two cases of the sample directly illuminated through the excitation beam path in the integrating sphere; and also the case of the empty sphere. A Time Correlated Single Photon Counting (TCSPC) detector and a pulsed ultraviolet laser diode ($\lambda = 374$ nm) were used to acquire time-resolved PL spectra. An instrument response function of $\Delta t = 0.13$ ns provides a limit to the overall time resolution. Time-resolved emission spectra were recorded by measuring individual transient PL traces at increasing emission wavelengths. Ultraviolet–visual absorption was measured using a LAMBDA 950 UV/Vis/NIR spectrometer.

Femtosecond TA measurement. A Yb:KGW regenerative amplifier (Pharos, Light Conversion) produced the 1,030 nm fundamental (5 KHz). A portion of the beam was passed through an optical parametric amplifier (Orpheus, Light Conversion) to generate the 3.8 eV pump pulse. Both the pump pulse and residual fundamental were sent into an optical bench (Helios, Ultrafast). The fundamental was sent through a delay stage, which determines the time delay between the two pulses, and then was focused into a sapphire crystal, generating a white light continuum. The pump pulse was sent through an optical chopper, reducing its frequency to 2.5 kHz. Both beams were then focused onto the sample. The probe light reflected off the mirror and was directed toward a charge-coupled device (CCD, Helios, Ultrafast).

XPS and UPS measurements. XPS and UPS measurements were conducted using the PHI5500 multi-technique system with a base pressure of about 10^{-9} torr. The X-ray radiation was Al Kα emission (1486.7 eV, take-off angle 75 degrees). The ultraviolet radiation used in the UPS is helium Iα radiation, which has a photon energy of 21.22 eV. The take-off angle was 88 degrees. A bias of –15 V was applied to measure the UPS spectra.

Characterization. AFM measurements were performed with an Asylum Research Cypher AFM operated in alternating-current mode in ambient air. Imaging was carried out using ASYELEC-02 silicon probes with titanium-iridium coatings from Asylum Research. The probes had a typical spring constant of 42 N m^{-1}. A JEOL JEM 2100 TEM was used to investigate the morphologies of the HCP-DB-CDs. X-ray powder diffraction patterns were carried out using Cu-Kα radiation (PANalytical X'Pert Pro MPD). Attenuated total reflectance Fourier transform infrared measurements were performed on a Thermo Nicolet is50. The Raman spectrum was measured using Laser Confocal Micro-Raman Spectroscopy (LabRAM Aramis). Low-temperature-dependent PL spectra measurements were performed in the temperature range 90–300 K using liquid nitrogen cooling.

Theoretical calculations. Bandgap fluctuation studies were performed using the Perdew–Burke–Ernzerhof exchange-correlation functional using the projected augmented wave pseudopotentials as implemented in the computational package VASP[50]. The atomic displacements and the resulting bandgap change were obtained from molecular dynamics simulations at a temperature of 300 K with a time step of 1 fs. The atoms were initially allowed to equilibrate for 200 time steps before the collection of final data.

Device fabrication and characterization. Low-conductivity ITO-coated glass substrates were cleaned by sonicating in deionized water and then in organic solvents (acetone then isopropyl alcohol), and then dried in an oven at 120 °C for 10 min. The substrates were cleaned using an ultraviolet-plasma treatment to enrich the ITO surface with oxygen and increase the ITO work function. The poly(3,4-ethylenedioxythiophene): poly(styrenesulfonate) (PEDOT:PSS) hole injection layer was spin-coated at 6,000 rpm (acceleration speed is 6,000 rpm) for 20 s on the ITO followed by annealing in a nitrogen-filled glovebox at 150 °C for 30 min. Subsequently, TFB dissolved in chlorobenzene (5 mg ml^{-1}) solution was spin-coated on top of the PEDOT:PSS layer at 5,000 rpm (acceleration speed is 5,000 rpm) for 30 s, and annealed at 150 °C for 30 min in a nitrogen-filled glovebox. The emissive layer of HCP-DB-CDs blended with PVK at different concentrations were spin-coated at 3,000 rpm (acceleration speed is 500 rpm) for 45 s on the surface of the TFB film, followed by annealing in a nitrogen-filled glovebox at 100 °C for 10 min. Finally, the substrates were transferred to a vacuum chamber, and TPBI (60 nm) and LiF/Al electrodes (1 nm/150 nm) were deposited using a Kurt J. Lesker LUMINOS Cluster Tool evaporation system through a shadow mask under a high vacuum of less than 10^{-4} Pa. The device active area was 6.14 mm^2 as defined by the overlapping area of the ITO and Al electrodes. The luminance–current density–voltage characteristics were collected by using a HP4140B picoammeter. The absolute EL power spectra of the devices were collected using an integrating sphere and an Ocean Optics USB4000 spectrometer by mounting the devices on the wall of the integrating sphere. The EQEs were then calculated from the measured absolute power spectra and the current density.

Data availability

The data that support the findings of this study are available from the corresponding author upon reasonable request.

References

50. Kresse, K. et al. Efficient iterative schemes for ab initio total-energy calculations using a plane-wave basis set. *Phys. Rev. B* **54**, 11169 (1996).

Acknowledgements

This work is supported by Tier 1 Canada Research Chair in Organic Optoelectronics (grant number 950-220944), the Natural Sciences and Engineering Research Council of Canada (NSERC, grant number 216956-12), and the National Natural Science Foundation of China (grant number 11774304). E.H.S. and all coauthors from the Department of Electrical and Computer Engineering at the University of Toronto acknowledge financial support from the Ontario Research Fund–Research Excellence Program and from the Natural Sciences and Engineering Research Council of Canada (NSERC). M.I.S. acknowledges the support of the Banting Postdoctoral Fellowship Program, administered by the Government of Canada. Computations were performed on the Niagara supercomputer at the SciNet HPC Consortium. SciNet is funded by the Canada Foundation for Innovation; the Government of Ontario; Ontario Research Fund-Research Excellence; and the University of Toronto.

Author contributions

Z.-H.L. and E.H.S. supervised the project. F.Y. conceived the idea and designed the experiments. F.Y. prepared the samples and fabricated devices. Y.-K.W. conducted the AFM characterization and helped prepare the figure sets. O.V., G.S. and K.S. conducted the density functional theory calculations. X.Z. and O.M.B. provided useful suggestions and helped with the manuscript revision. Y.D. and G.B. measured the femtosecond TA spectra. P.L. and H.K. measured the UPS and XPS. A.J. measuerd the temperature-dependent PL. J.Z.F. measured the FITR spectra. B.C. measured the SEM image. F.Y. wrote the first draft of the manuscript. Z.-H.L., O.V. and E.H.S. provided major revisions. All authors discussed the results and contributed to the manuscript.

Competing interests

The authors declare no competing interests.

Additional information

Extended data is available for this paper at https://doi.org/10.1038/s41566-019-0557-5.

Supplementary information is available for this paper at https://doi.org/10.1038/s41566-019-0557-5.

Correspondence and requests for materials should be addressed to Z.-H.L. or E.H.S.

Reprints and permissions information is available at www.nature.com/reprints.

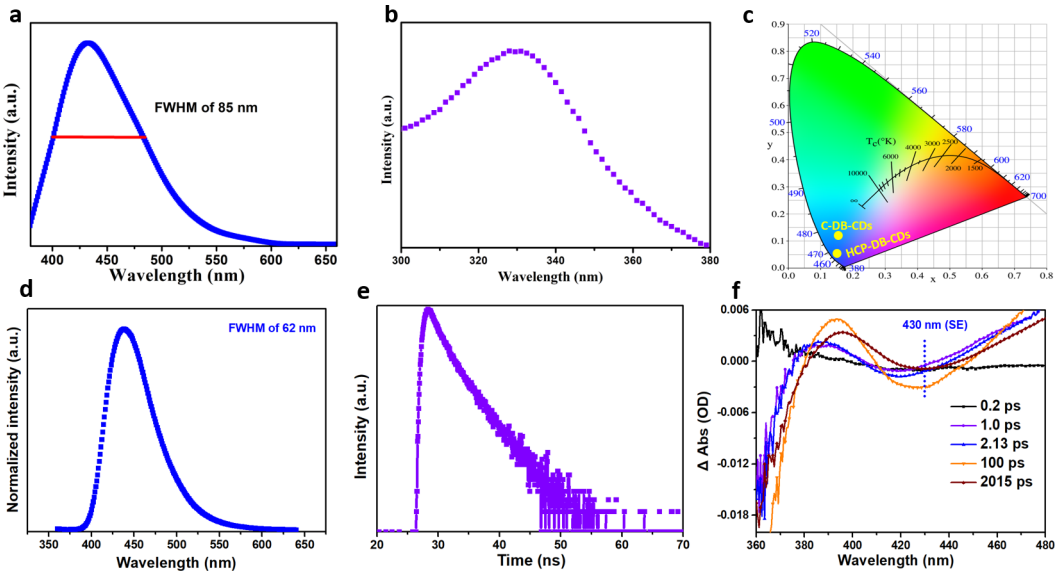

Extended Data Fig. 1 | Optical properties of C-DB-CDs. a, **b**, **e**, **f**, PL spectra (**a**), absorption spectra (**b**), time-resolved PL spectra (**e**) and femtosecond TA spectra (**f**) of C-DB-CDs. **c**, Colour coordinates of the emission spectra of C-DB-CDs and HCP-DB-CDs. **d**, PL spectra of C-DB-CDs treated at 200 °C for 1h without the addition of amination reagents.

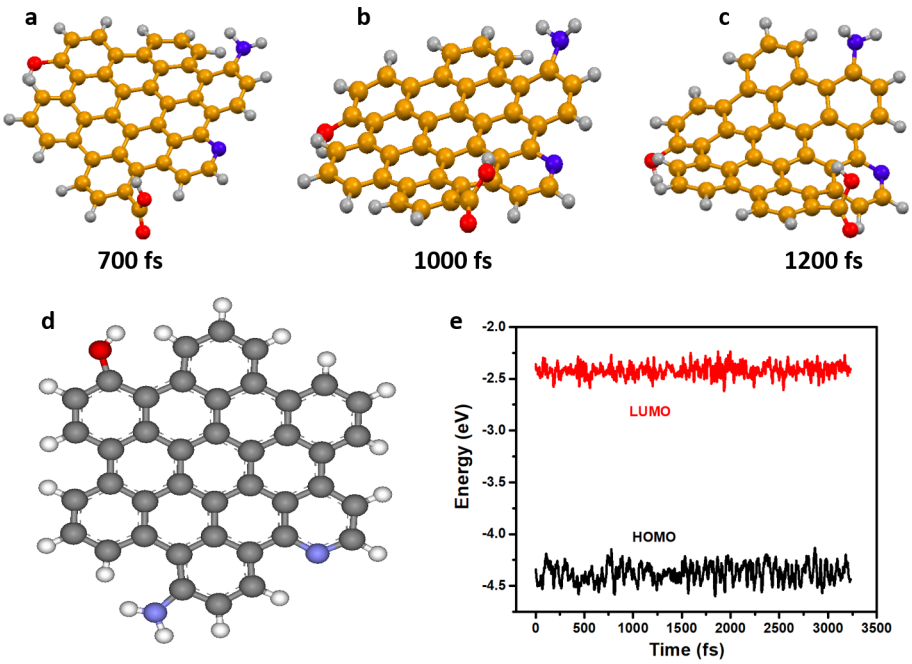

Extended Data Fig. 2 | Density functional theory calculations on model CDs. a, **b**, **c**, The geometries of COOH-CD at different time intervals, such as 700 fs (**a**), 1,000 fs (**b**) and 1,200 fs (**c**), respectively. **d**, **e**, The structure (**d**) and bandgap fluctuations (**e**) of model CDs functionalized with different functional groups such as OH and NH_2 without COOH.

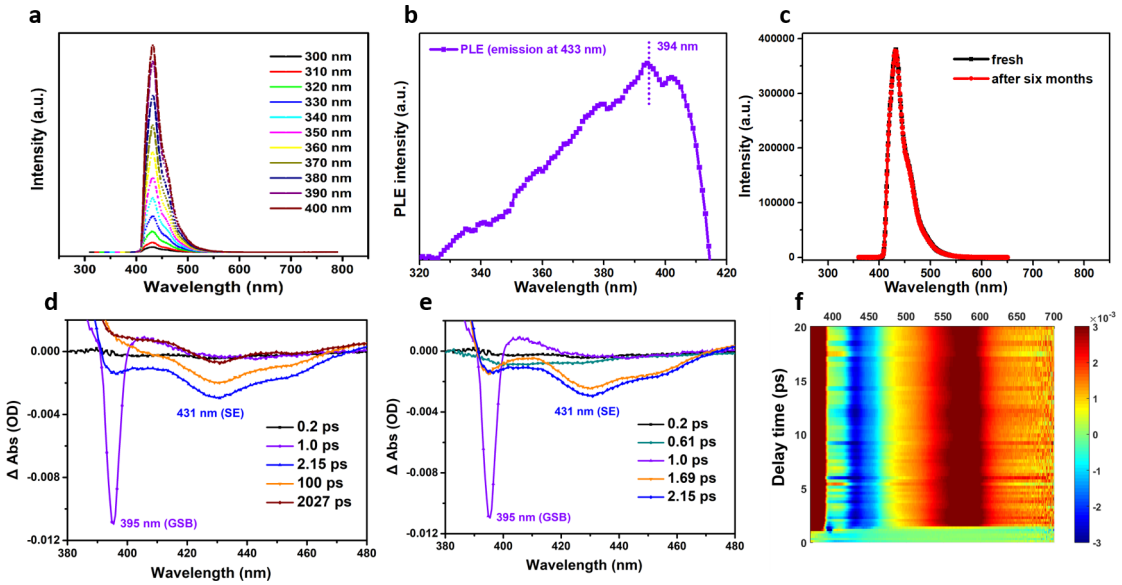

Extended Data Fig. 3 | Optical properties of HCP-DB-CDs. a, PL spectra of HCP-DB-CDs excited at different wavelengths. **b**, PL excitation spectra of HCP-DB-CDs with emission at 433 nm. **c**, PL spectra of HCP-DB-CDs measured in the fresh state and after storing for six months in ambient conditions. **d**, **e**, Time evolution of femtosecond TA spectra in the time range from 0.2 ps to 2,027 ps (**d**) and from 0.2 ps to 2.15 ps (**e**), excited at 355 nm. **f**, Two-dimensional pseudocolour map of TA spectra of HCP-DB-CDs expressed in ΔOD (the change of the absorption intensity of the sample after excitation) as a function of both delay time (from 0 to 20 ps) and probe wavelength excited at 355 nm.

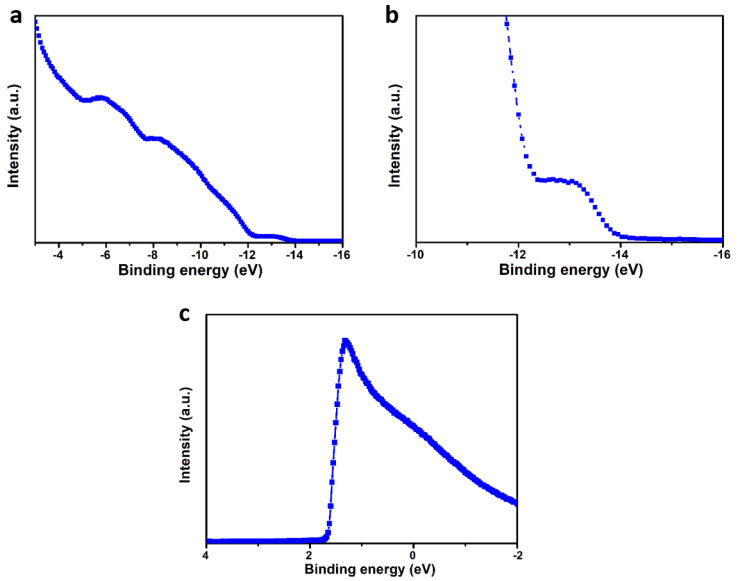

Extended Data Fig. 4 | UPS data of HCP-DB-CDs. a, **b**, Valence band spectrum of HCP-DB-CDs in the binding energy range from –3 eV to –16 eV (**a**) and from –10 eV to –16 eV (**b**). **c**, Secondary electron spectrum of HCP-DB-CDs.

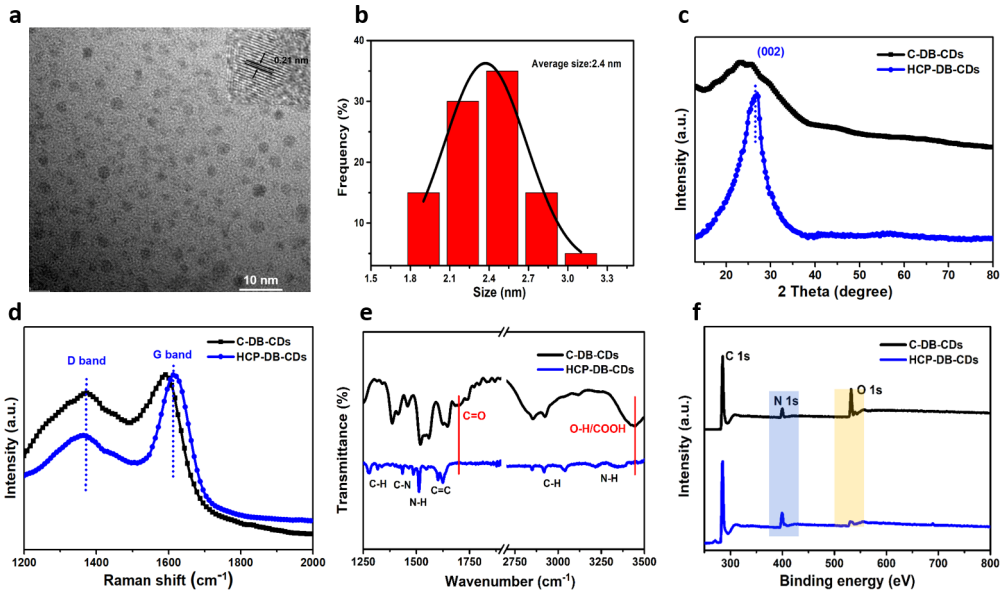

Extended Data Fig. 5 | Structural characterization of HCP-DB-CDs and C-DB-CDs. a, **b**, TEM image (**a**) (inset is the corresponding high-resolution TEM image), and the size distribution (**b**) of HCP-DB-CDs. **c**, **d**, **e**, **f**, Comparison of X-ray powder diffraction patterns (**c**), Raman spectra (**d**), Fourier transform infrared spectra (**e**) and XPS full spectra (**f**) of HCP-DB-CDs and C-DB-CDs.

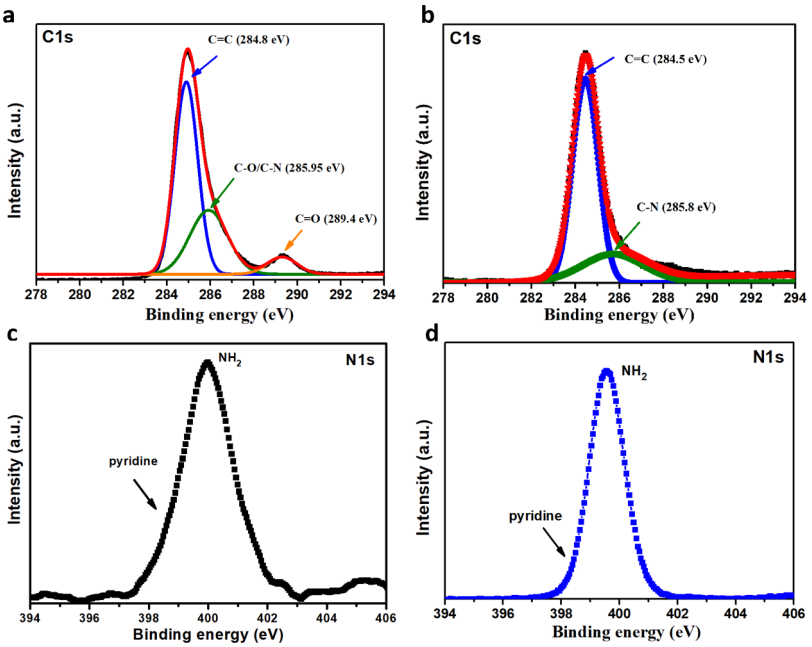

Extended Data Fig. 6 | High-resolution C1s and N1s XPS spectra of HCP-DB-CDs and C-DB-CDs. a, **b**, High-resolution C 1s XPS spectra of C-DB-CDs (**a**) and HCP-C-DB-CDs (**b**). **c**, **d**, High-resolution N 1s XPS spectra of C-DB-CDs (**c**) and HCP-C-DB-CDs (**d**).

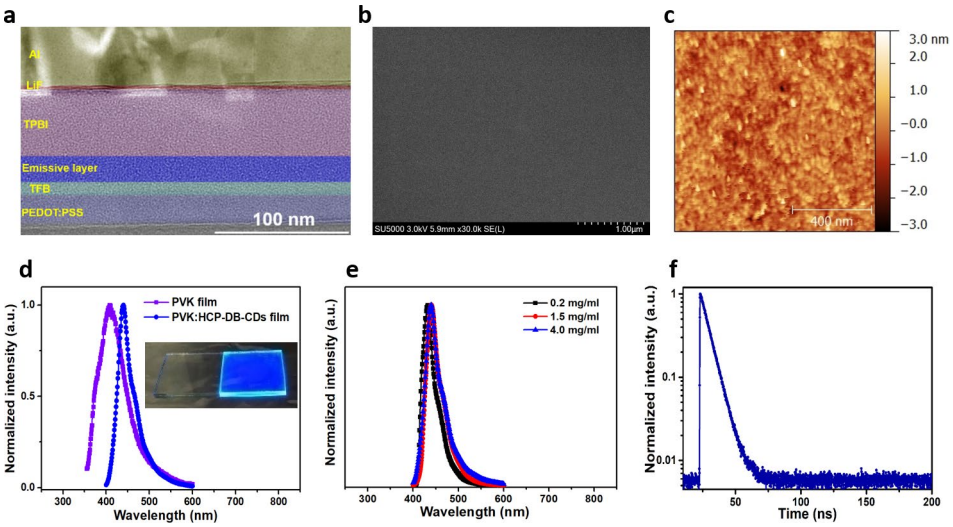

Extended Data Fig. 7 | Cross-sectional TEM image of LEDs and film properties of the active emission layer. a, Cross-sectional TEM image of the HCP-DB-CD-based LEDs. **b**, **c**, SEM image (**b**) and AFM height image (**c**) of the active emission layer of PVK:HCP-DB-CDs film. **d**, PL spectra of PVK and PVK:HCP-DB-CD films. (Insets are the photographs of two films under ultraviolet light). **e**, Comparison of the PL spectra of PVK:HCP-DB-CD films (HCP-DB-CDs are dispersed in the polymer PVK with the concentration in the range 1.5–4 mg ml^{-1}) and HCP-DB-CDs solution. **f**, Time-resolved PL spectra of PVK:HCP-DB-CDs film.

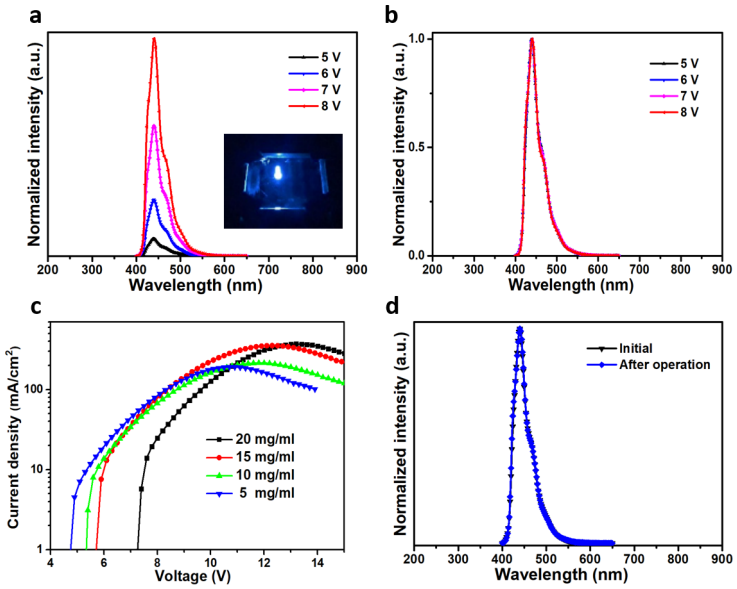

Extended Data Fig. 8 | EL properties and current density curves as a function of applied voltage for the HCP-DB-CD-based LEDs. a, **b**, EL spectra (**a**) and normalized EL spectra (**b**) of HCP-DB-CD-based LEDs at different operation voltage. (Inset is the operation photograph of the HCP-DB-CD-based LEDs operated at 7 V). **c**, Current density curves as a function of applied voltage for the HCP-DB-CD-based LEDs prepared with different concentrations of PVK:HCP-DB-CDs. **d**, Normalized EL spectra before and after operation for three hours.

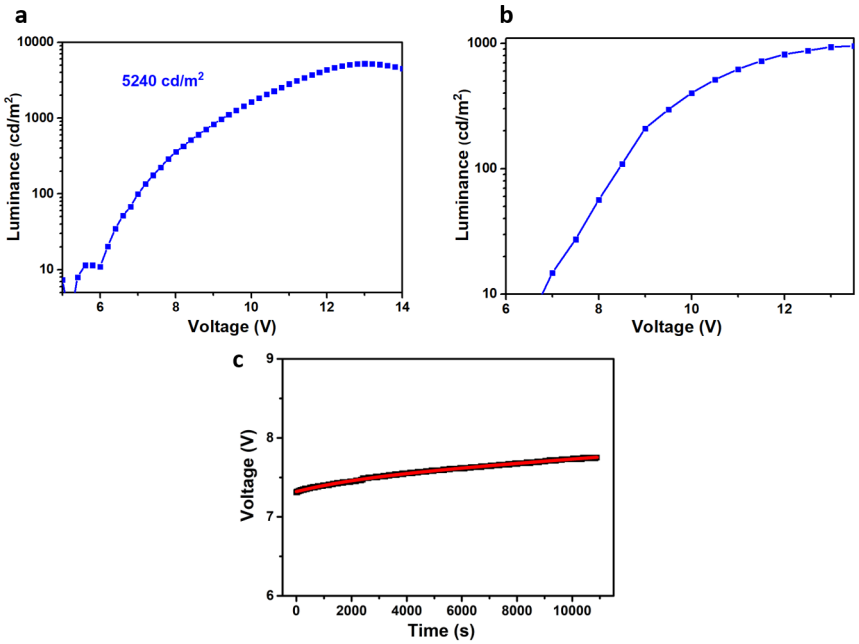

Extended Data Fig. 9 | Luminance-voltage characteristic and driving voltages for the HCP-DB-CD-based LEDs versus operation time. a, Luminance–voltage characteristic of HCP-DB-CD-based deep-blue LEDs with maximum brightness of 5,240 cd m^{-2} (The concentration of TFB was 3.5 mg ml^{-1} for spin-coating to form a hole-transport layer). **b**, Luminance–voltage characteristic of HCP-DB-CD-based deep-blue LEDs with maximum brightness of 954 cd m^{-2} (without the TFB hole-transport layer). **c**, Driving voltages for the HCP-DB-CD-based LEDs versus operation time under ambient conditions with constant driving current density of 40 mA cm^{-2}.

Device structure	Emission peak (nm)	Current efficiency (cd/A)	EQE (%)	Brightness (cd m^{-2})	Reference
ITO/PVK:CDs/TPBi/LiF/Al	474	NA	NA	570	*Adv. Opt. Mater.* **6**, 1800181 (2018)
ITO/PEDOT:PSS/P-TPD/CDs/TPBi/LiF/Al	430	0.03	NA	30	*ACS Nano* **7**, 11234-11241 (2013)
ITO/GraHIL/GQDs:CBP/TPBi/LiF/Al	500	0.06	0.1	10	*Nano Lett.* ***14***, 1306-1311 (2014)
ITO/PEDOT:PSS/CQDs/TPBi/Ca/Al	455	0.084	NA	136	*Adv. Mater.* ***29***, 1604436 (2017)
ITO/PEDOT:PSS/PVK:CQDs/TPBi/Ca/Al	510	5.11	NA	4672	*Nat. Comm.* ***9***, 2249 (2018)
ITO/PEDOT:PSS/P-TPD/PVK:CQDs/TPBi/Ca/Al	626	2.19	NA	2700	*Adv. Sci.* ***6***, 1900397 (2019)
ITO/PEDOT:PSS/TFB/PVK:CDs/TPBi/LiF/Al	**433**	**2.6**	**4.04**	**5240**	**This work**

Extended Data Fig. 10 | Comparison of the device structure and performance of CD-based LEDs for previously reported works relative to the present work.